

MATERIALS SCIENCE

Self-driving laboratory for accelerated discovery of thin-film materials

B. P. MacLeod^{1,2*}, F. G. L. Parlane^{1,2*}, T. D. Morrissey^{1,2}, F. Häse^{3,4,5,6}, L. M. Roch^{3,4,5,6}, K. E. Dettelbach¹, R. Moreira¹, L. P. E. Yunker¹, M. B. Rooney¹, J. R. Deeth¹, V. Lai¹, G. J. Ng¹, H. Situ¹, R. H. Zhang¹, M. S. Elliott¹, T. H. Haley¹, D. J. Dvorak², A. Aspuru-Guzik^{3,4,5,6,7†}, J. E. Hein^{1†}, C. P. Berlinguette^{1,2,7,8†}

Discovering and optimizing commercially viable materials for clean energy applications typically takes more than a decade. Self-driving laboratories that iteratively design, execute, and learn from materials science experiments in a fully autonomous loop present an opportunity to accelerate this research process. We report here a modular robotic platform driven by a model-based optimization algorithm capable of autonomously optimizing the optical and electronic properties of thin-film materials by modifying the film composition and processing conditions. We demonstrate the power of this platform by using it to maximize the hole mobility of organic hole transport materials commonly used in perovskite solar cells and consumer electronics. This demonstration highlights the possibilities of using autonomous laboratories to discover organic and inorganic materials relevant to materials sciences and clean energy technologies.

INTRODUCTION

Optimizing the properties of thin films is time intensive because of the large number of compositional, deposition, and processing parameters available (1, 2). These parameters are often correlated and can have a profound effect on the structure and physical properties of the film and any adjacent layers present in a device (3). There exist few computational tools for predicting the properties of materials with compositional and structural disorder, and thus, the materials discovery process still relies heavily on empirical data. High-throughput experimentation (HTE) is an established method for sampling a large parameter space (4, 5), but it is still nearly impossible to sample the full set of combinatorial parameters available for thin films. Parallelized methodologies are also constrained by the experimental techniques that can be used effectively in practice. The overwhelming size of the thin-film materials parameter space motivates the need for both data- and theory-guided algorithms for executing experiments beyond what can be achieved with HTE alone (6–8).

The experimental approach of iterating between automated experimentation and machine learning–based experiment planning has resulted in early successes in addressing high-dimensional problems in experimental physics (9), chemistry (10), and life sciences (11). This approach is only starting to be implemented in the materials sciences (1), as demonstrated by the optimization of carbon nanotube growth (12), amorphous alloy compositions (13), and in-

organic perovskite quantum dot nucleation (7). We demonstrate here the optimization of thin films using our platform named “Ada,” a flexible and modular self-driving laboratory capable of autonomously synthesizing, processing, and characterizing organic thin films (Fig. 1, fig. S1, and movie S1). Ada trains itself how to find target parameters without any prior knowledge, enabling iterative experimental designs that maximize the information gain per sample (Fig. 2).

RESULTS

As a first step in proving out the methodology, we designed Ada to target organic hole and electron transport layers that are ubiquitous in advanced solar cells (14), as well as optoelectronics applications such as organic lasers (15) and light-emitting diodes (16). For this work, we configured Ada specifically to optimize the hole mobility of spiro-OMeTAD, an organic hole transport material (HTM) common to perovskite solar cells (PSCs) (17). The hole mobility of spiro-OMeTAD is critical to PSC performance, but it is highly sensitive to dopants, additives, spin coating solvents, and postdeposition processing (17–24). How each of these factors affect the hole mobility of amorphous spiro-OMeTAD remains difficult to model (3, 25), and thus, optimizing the relevant properties of spiro-OMeTAD is still done empirically. This optimization process often takes months to complete and slows the translation of new organic hole and electron transport layers for solar cells and related devices.

Ada autonomously optimizes the hole mobility of spiro-OMeTAD by (i) measuring and mixing solutions of HTMs, dopants, and plasticizers; (ii) depositing solutions as thin films on rigid substrates; (iii) annealing each film for a specified duration; (iv) imaging each film to detect morphologies, defects, and impurities; and (v) characterizing the optical and conductivity properties to produce surrogate hole mobility data. These data are received by ChemOS (26), which uses the Phoenix (27) global Bayesian optimization algorithm to design new experiments by actively learning from previously acquired data. Phoenix uses a sampling parameter to explicitly bias experimental design toward exploration or exploitation in an

¹Department of Chemistry, The University of British Columbia, Vancouver, British Columbia, Canada. ²Stewart Blusson Quantum Matter Institute, The University of British Columbia, Vancouver, British Columbia, Canada. ³Department of Chemistry and Chemical Biology, Harvard University, Cambridge, MA, USA. ⁴Department of Chemistry, University of Toronto, Toronto, Ontario, Canada. ⁵Department of Computer Science, University of Toronto, Toronto, Ontario, Canada. ⁶Vector Institute for Artificial Intelligence, MaRS Centre, Toronto, Ontario, Canada. ⁷Canadian Institute for Advanced Research (CIFAR), MaRS Centre, Toronto, Ontario, Canada. ⁸Department of Chemical and Biological Engineering, The University of British Columbia, Vancouver, British Columbia, Canada.

*These authors contributed equally to this work.

†Corresponding author. Email: cberling@chem.ubc.ca (C.P.B.); alan@aspuru.com (A.A.-G.); jhein@chem.ubc.ca (J.E.H.)

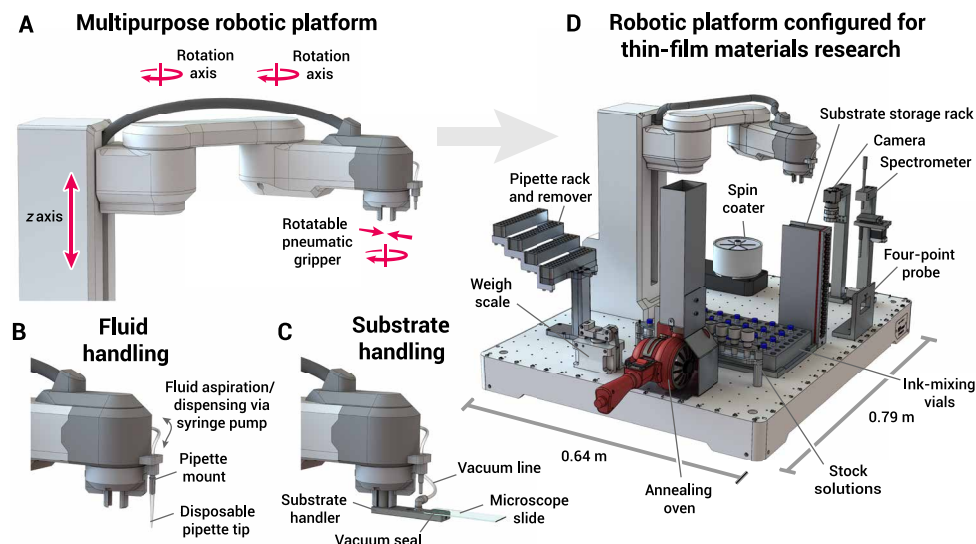


Fig. 1. The Ada self-driving laboratory. (A) The self-driving laboratory is based on a modular robotic platform that interacts with objects using a rotatable pneumatic gripper on a polar robotic arm achieving 10- μm repeatability and a maximum velocity of ~ 1 m/s. (B) Fluid handling is achieved using disposable pipette tips that can be press-fit onto and removed from the arm's pipette mount by the robot. Pipetting with a mean accuracy of 5 μl is achieved using a syringe pump connected to the pipette mount. (C) Substrate handling is achieved using a vacuum substrate handler gripped by the robotic arm. (D) Configuration of the robotic platform for a specific experimental workflow is achieved by mounting an appropriate collection of experimental modules on the robot; here, the Ada platform is shown equipped for the synthesis and characterization of thin-film materials.

alternating fashion and has been shown to outperform random and systematic searches (26–28). The optimization experiments are performed by a multipurpose robot (Fig. 1) equipped with a rotatable, pneumatic gripper and a pipette mount that enable the platform to accomplish a wide variety of tasks by interacting with a number of different modules. The platform aspirates, dispenses, and mixes liquid precursors with the assistance of a syringe pump and a weigh scale. Precursor solutions are spin-cast as thin films on glass substrates, which can then be annealed up to 165°C (fig. S2) using a forced convection annealing system that enables control over the extent of annealing by leveraging the ability of the robot to accurately and repeatedly position the sample in a hot air stream for a precisely controlled duration. Ada then characterizes the films using purpose-built systems for dark-field photography, ultraviolet-visible–near-infrared (UV-vis-NIR) reflection and transmission spectroscopy, and four-point probe conductance. The robot also serves as an XYZ sample positioning stage enabling all characterizations to be performed at multiple positions on the sample, which we leverage to collect spectroscopy and conductance data at seven spatial positions on each sample. One sample is synthesized and characterized approximately every 20 min, with consumables (pipettes, substrates, and stock solutions) requiring replenishment every seven samples. The ability to produce high-quality, well-organized datasets (figs. S3 and S4) while also enabling typically uncontrolled variables (e.g., time between process steps and height of spin coating dispense nozzle) to become controlled or optimization parameters are very powerful features of Ada. Moreover, Ada is controlled using flexible, open-source Python software (see Materials and Methods), which facilitates the rapid implementation of new experiments.

We selected HTM hole mobility as our target property for optimization, but this property typically requires assembly of multilayer devices to get a valid measurement (25, 29, 30). Conventional methods are simply not compatible with the time scale needed for

efficient autonomous optimization (31). We therefore developed a scheme where we could use four-point probe conductivity and UV-vis-NIR spectroscopy measurements to produce a diagnostic quantity, pseudomobility, that is proportional to hole mobility (see Materials and Methods and fig. S5). Pseudomobility is the quotient of the sheet conductance of a thin film and the absorbance of oxidized spiro-OMeTAD in the film. We estimated the absorbance of each thin film with an analytical model that incorporates experimental reflection and transmission spectra and accounts for the effect of the glass substrate on these spectra. The pseudomobility ratio, which provides a thickness-independent, low-latency, analytical surrogate for hole mobility, became our target optimization objective and enabled us to accelerate the rate of meaningful data collection.

The pseudomobilities of spiro-OMeTAD thin films were optimized by iteratively designing film compositions with variable annealing times and dopant concentrations (Fig. 2, tables S1 and S2). Solutions prepared from stock solutions of spiro-OMeTAD and a cobalt(III) dopant (along with a fixed amount of the plasticizer 4-*tert*-butylpyridine) were spin-coated onto substrates to yield thin films. Each film was annealed, imaged, and analyzed to determine a pseudomobility value that was relayed to ChemOS. Figure 3A chronicles how the doping ratios and annealing times were varied during optimization for two independent experimental campaigns. Each of the two 35-sample campaigns took under 30 hours (including time for restocking consumables), and each had one failed sample. This failure rate is typical for our system. An important outcome is that both campaigns converged on the same global maximum for both doping ratio (~ 0.4 equivalents) and annealing time (~ 75 s) to deliver films with the same maximum pseudomobilities. This reproducible endpoint demonstrates that Ada can successfully navigate a broad experimental space (see table S3 for additional reproducibility data).

Figure 3B shows the locations and sequence of the experimentally sampled points in the parameter space. The sampled points can be

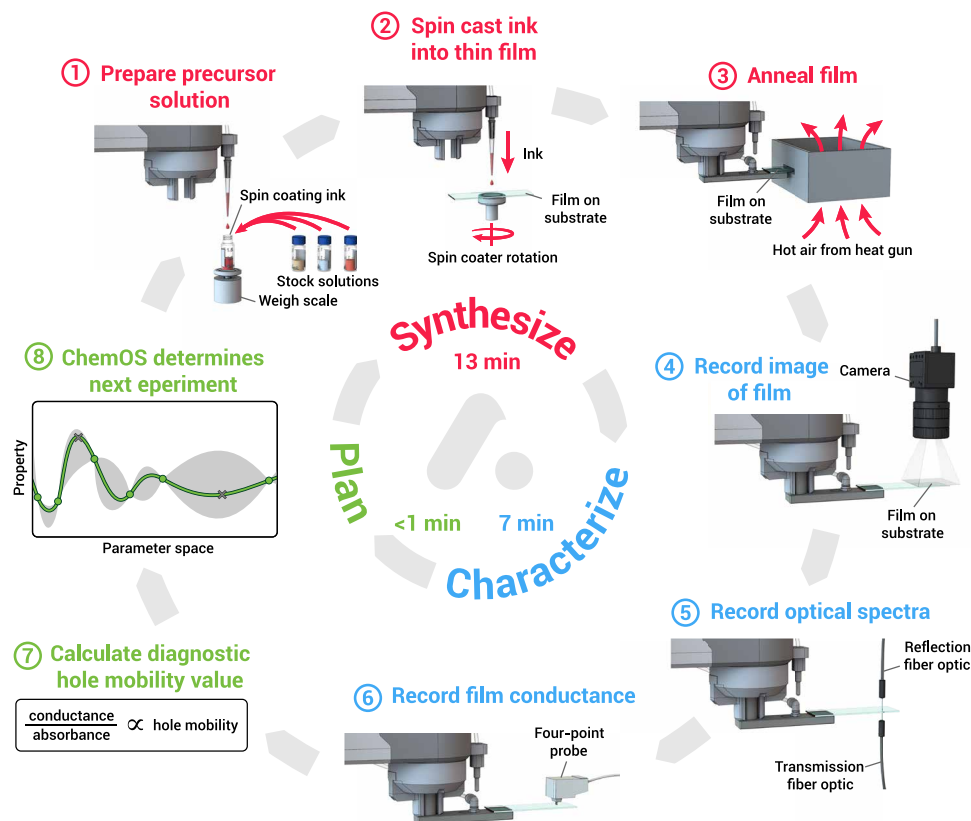


Fig. 2. Ada uses an autonomous optimization workflow. The autonomous workflow involves iterative experimentation with the goal of discovering a thin-film composition with the highest possible pseudomobility. Each iteration of the workflow involves the following: (1) mixing an hole transport material (HTM)-dopant-additive ink, (2) spin coating the ink onto a substrate, (3) thermally annealing for a variable amount of time, (4) imaging with a visible-light camera, (5) acquiring ultraviolet-visible-near-infrared (UV-vis-NIR) spectra in reflection and transmission modes, (6) measuring the current-voltage (*I*-*V*) curve of the film with a four-point probe, (7) computing a pseudomobility based on the *I*-*V* and spectroscopic data, and (8) feeding this pseudomobility into the ChemOS (14) orchestration software and the Phoenix Bayesian optimization algorithm (15), which then designs the next experiment.

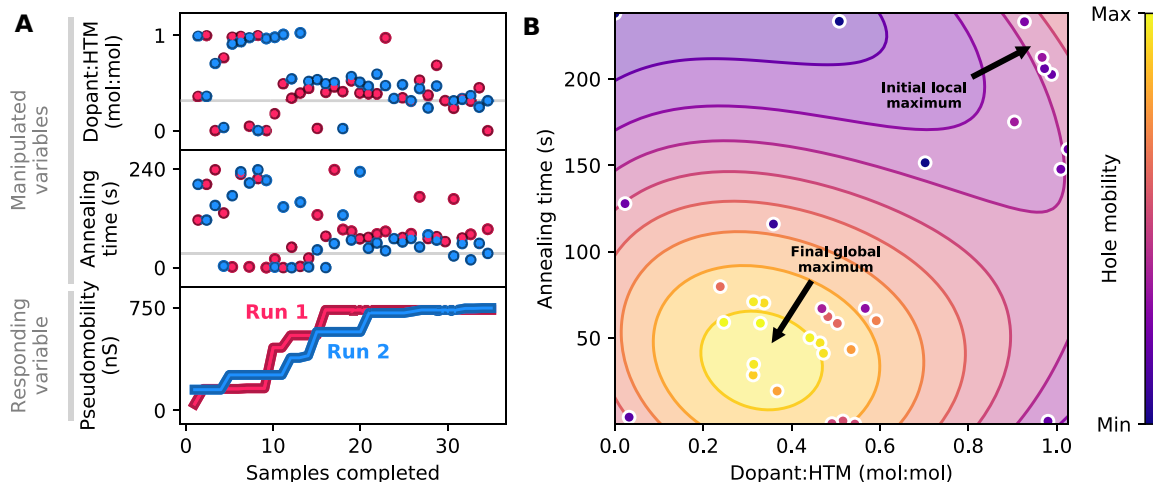


Fig. 3. Results of thin-film pseudomobility optimization carried out by the self-driving laboratory. (A) Experimental values for cobalt doping ratio, annealing time, and maximum measured pseudomobility as a function of the number of experiments performed for two independent optimization runs. (B) The pseudomobility response surface and sampled points for the second (blue; left) optimization run. The algorithm initially found a local maximum and then found the global maximum of the sampled parameter space.

seen to initially cluster at a local maximum (~100% doping and annealing time >200 s) before finding a higher performance region elsewhere in the parameter space. While the eventual rejection of the local maximum confirms that the explore-exploit functionality of Phoenix can prevent the search from becoming stuck near local optima, we were curious why Ada identified a local maximum at high doping levels. Subsequent investigations of the dark-field images of these films revealed annealing-induced dewetting of the films containing intermediate amounts of dopant (fig. S6). At elevated doping levels, dewetting was suppressed, allowing a region of improved thermal stability to be identified (see the Supplementary Materials). The favorable performance of high-dopant/high-annealing time films was not intuitive (32), and this observation was facilitated by our autonomous platform, which searched over a larger range of doping and annealing conditions than is typically explored in studies of organic HTMs. We hypothesize that the highly doped films are stable at high annealing temperatures because of the greater intrinsic thermal stability of the dopant (which does not readily form a glass and melts at 189°C; see fig. S7) compared to amorphous spiro-OMeTAD [which exhibits a glass transition at 124°C; see (33)]. On this basis, when sufficient Co(III) salt is added to the HTM film, the increase in the stability of the doped HTM due to the intrinsic stability of the dopant overcomes the decrease in thermal stability generally associated with the addition of dopants to HTMs (32, 34, 35). This result is nontrivial and represents an unexpected scientific observation from an artificially intelligent experimental design.

DISCUSSION

We report here the first use of a self-driving laboratory to optimize composition and processing parameters for thin-film materials. This proof-of-principle study targeted the optimization of a type of thin organic semiconducting film common to advanced solar cells, but the modularity of our robotic platform and control software enables the rapid incorporation of new experiments, techniques, analytical hardware, and algorithms. The Ada platform can therefore be easily tailored for a range of inorganic and organic materials and applications and even be coupled to automated organic synthesis methodologies developed for the pharmaceutical industry (36, 37). The next stage of development for this robotic platform is to introduce sequential film deposition to extend autonomous optimization experiments to multilayered systems that comprise full devices. As the robotic workflow complexity increases, the experimental throughput of our current, fully serial scheme will decrease; to overcome this challenge, we plan to develop stand-alone synthesis and characterization modules that can run in parallel. Our ability to iteratively modify Ada will prove to be particularly useful in this regard. We expect platforms such as Ada to facilitate the deployment of effective autonomous experimentation at a scale compatible with the rapidly evolving needs and constraints (e.g., budget, time, and space) of a broad cross section of the materials science research community.

MATERIALS AND METHODS

Materials

Acetonitrile [CAS 75-05-8; high-performance liquid chromatography (HPLC) grade, ≥99.9%], toluene [CAS 108-88-3; American Chemical Society (ACS) grade], acetone (CAS 67-64-1; ACS grade), spiro-OMeTAD (CAS 207739-72-8; HPLC grade, 99%), FK 102

Co(III) bis(trifluoromethane)sulfonimide (TFSI) salt (Sigma-Aldrich, product number 805203; 98%), and 4-*tert*-butylpyridine (CAS 3978-81-2; 96%) were purchased from Sigma-Aldrich and were used without further purification. Extran 300 detergent (EX0996-1) and 2-propanol (ACS grade, ≥99.5%) were purchased from EMD Millipore Corporation and were used without further purification. Microscope slide substrates (75 mm by 25 mm by 1 mm; VWR, catalog no. 16004-430) were purchased from VWR International.

Consumables for the robotic platform

During the optimization experiments, the robotic platform was periodically restocked with consumables. These include microscope slides (3 inch by 1 inch by 1 mm; VWR VistaVision), 2-ml HPLC vials (Canadian Life Science), 200-μl pipettes (Biotix, M-0200-BC), and various stock solutions. Cleaning of the microscope slides and preparation of the stock solutions are further detailed below.

Manual preparation of stock solutions

All reagent solutions were prepared in an atmosphere dried over anhydrous calcium sulfate (DRIERITE), resulting in water (~0.005 mg/l) remaining in the atmosphere. Toluene (MePh) and acetonitrile (MeCN) solvents were prepared by drying over anhydrous magnesium sulfate, filtering through a 0.2-μm polytetrafluoroethylene filter, and stored over 3 Å molecular sieves. A solution of 1:1 (v/v) MeCN/MePh was prepared by mixing equal volumes of dry MeCN and MePh. A stock solution of spiro-OMeTAD was prepared by briefly (1 to 5 min) sonicating a mixture of spiro-OMeTAD (off-white powder) with MeCN/MePh. The resulting solution had a transparent, pale yellow color. A stock solution of FK 102 Co(III) TFSI salt was prepared by dissolving FK 102 Co(III) TFSI salt (bright orange crystalline powder) in MeCN/MePh and stored without exposure to UV light. The resulting solution had a transparent bright orange color. A stock solution of 4-*tert*-butylpyridine was prepared by dissolving *tert*-butylpyridine (clear, colorless solution) in MeCN/MePh. All stock solutions were prepared at concentrations of 50-mg solute per 1-ml solvent.

Manual cleaning of substrates

Microscope slide substrates (75 mm by 25 mm by 1 mm) were cleaned through multistep sonication. First, the slides were sonicated for 10 min in a 5% (v/v) solution of Extran in deionized water. The slides were then sonicated sequentially in deionized water, acetone, and 2-propanol for 10 min at each step. The slides were stored in 2-propanol and dried with filtered air before use.

Robotic methods

The robot used is a Selective Compliance Assembly Robot Arm-type robot (N9, North Robotics; www.northrobotics.com), which performs the robotic manipulations in our workflows. This robot is driven by a controller (C9, North Robotics), which also provides auxiliary controls for third-party instruments and components used by the robot. The controller and additional peripherals are controlled by a computer running a Python script based on open-source libraries (see <https://gitlab.com/ada-chem>).

Autonomous workflow step 1: Robotic preparation of spin coating inks

The precursor solution for each sample was prepared by mixing varying amounts of spiro-OMeTAD stock solution, FK 102 Co(III)

TFSI salt stock solution, and 4-*tert*-butylpyridine stock solution in ambient conditions. In each precursor solution, the FK 102 Co(III) TFSI:spiro-OMeTAD ratio (n/n) was between 0 and 1, with the ratio determined by the ChemOS orchestration software. The ratio (m/m) of *tert*-butylpyridine to the total amount of spiro-OMeTAD and FK 102 Co(III) TFSI was fixed at 0.2. The resulting precursor solutions became dark purple in appearance upon the combination of the spiro-OMeTAD and FK 102 Co(III) TFSI solutions. The precursor solutions were mixed through aspiration and were used within a minute of preparation.

Autonomous workflow step 2: Robotic spin coating of thin-film samples

The thin-film samples were prepared via spin coating with a custom-built spin coater provided by North Robotics. The microscope slides were spun at 1000 rpm, and 0.100 ml of the precursor solution was dispensed at a normal incidence at the center of the slide. Rotation continued for 60 s.

Autonomous workflow step 3: Robotic thermal processing of thin-film samples

The forced convection annealing furnace was constructed from an MHT Products Inc. model 750 heat gun facing upward into a vertically oriented rectangular aluminum tube (75 mm by 50 mm) kept under ambient conditions. A sample port (40 mm by 5 mm) was cut 40 mm from the heat gun. Freshly spin-coated thin-film samples were moved using the N9 slide gripper into the furnace via the sample port, after which the heat gun power was triggered for the amount of time requested by the orchestration software. The temperature profile of the annealing procedure is shown in fig. S2. The temperature of the slide ramps from ambient temperature to 165°C over the first 100 s and remains at that temperature for the rest of the annealing time. After the requested heating time elapsed, the arm immediately removed the sample from the furnace and held it 25 mm above a 4500 rpm cooling fan for 3 min. This cooling period allowed samples to return to ambient temperature, regardless of annealing time, before further characterization.

Autonomous workflow step 4: Robotic dark-field photography

Thin-film samples were imaged at a dark-field photography station composed of a FLIR Blackfly S Mono 12 MP USB Vision (Sony IMX226) camera mounted above an AmScope MIC-209 3-W ring light. The sample was moved by the robotic arm to 90 mm below the camera and was illuminated by the ring light to provide contrast between smooth and rough regions of the film. Images were captured at three different overlapping locations at a resolution of 4000 pixels by 3000 pixels. Manual postexperiment analysis of collected images was used to identify dust, defects, and dewetting in thin-film samples.

Autonomous workflow step 5: Robotic UV-vis-NIR spectroscopy Spectrometer design

UV-vis-NIR transmission and reflection spectra were collected with a custom-built, fiber-optic spectroscopy station. A BLACK-Comet UV-vis spectrometer (190 to 900 nm, <1-nm resolving resolution), a DWARF-Star miniature NIR spectrometer (900 to 1700 nm, 2.5-nm resolving resolution), and two SL4 high-power tungsten halogen and deuterium lamps (190- to 2500-nm spectral range, 3000 K) were

purchased from StellarNet Inc. The visible portions of the lamps were operated on the third color temperature setting. A three-way split fiber-optic reflection probe was positioned above and normal to the surface of the sample, which was connected to the BLACK-Comet spectrometer, the DWARF-Star spectrometer, and an SL4 lamp (reflection lamp). A collimating lens was positioned below and normal to the surface of the sample and was connected to the second SL4 lamp (transmission lamp) via a second fiber-optic cable. A mechanical shutter was placed between the collimating lens and the sample, which was darkened with black flocked paper (Thorlabs, part number BFP1). The BLACK-Comet UV-vis and DWARF-Star miniature NIR spectrometers were controlled using a Raspberry Pi 3 Model B+ (2017) running Raspbian Stretch (kernel 4.14) and Python 2.7.0. The SL4 lamps were controlled using an Arduino Due (A000062), which was slaved to the Raspberry Pi.

To perform a transmission measurement, the mechanical shutter was opened, the upper reflection lamp internal shutter was closed, and the lower transmission lamp internal shutter was opened. To perform a reflection measurement, the mechanical shutter was closed, the lower transmission lamp internal shutter was closed, and the upper reflection lamp internal shutter was opened.

Spectrometer calibration

A glass slide (75 mm by 25 mm by 1 mm) coated with 50-nm aluminum was purchased from Deposition Research Laboratory Inc. for use as a reflectance baseline. The true specular reflectance of the prepared reference sample was measured with an Agilent Cary 7000 Universal Measurement Spectrophotometer using the Cary Universal Measurement Accessory to hold the sample at 10° from normal. The sensitivity of the BLACK-Comet and DWARF-Star spectrometers were set by increasing the integration time (in milliseconds) of the detectors until the signal was between 80 and 95% of saturation, where saturation was 2^{16} counts. For transmission measurements, the sensitivity was determined with no sample present, and for reflection measurements, the sensitivity was determined with the calibrated aluminum mirror. The bright and dark baselines for transmission were completed with no sample present and with the transmission lamp on and off, respectively. The bright and dark baselines for reflection were completed with the calibrated aluminum mirror present and with the reflection lamp on and off, respectively. The known true reflection of the aluminum mirror, obtained from the Cary 7000, was used to define the bright reflection baseline.

Robotic spectroscopy measurement

For each film fabricated by the robotic platform, UV-vis-NIR spectra were collected by the robot, which holds samples in the optical path of the spectrometer using the vacuum substrate handler. First, the reflection and transmission spectra of a blank glass substrate were collected, followed by analogous reflection and transmission spectra of the annealed thin film on an identical substrate. The spectra of the uncoated and coated substrate were used to compute an approximation to the absorbance of the thin film, as described in the UV-vis-NIR data processing section. The spectra of each thin film and the spectra of the blank substrate were measured at seven positions spaced ~1 mm apart near the center of the substrate.

UV-vis-NIR data processing

Reflection and transmission spectra were measured at normal incidence and were assumed to be entirely specular and incoherent. This assumption is reasonable as long as surfaces and interfaces scatter a minimal amount of light and interference fringes in the spectra are minimal. At any wavelength/energy, the raw reflection

(R_0) and transmission (T_0) of the blank substrate can thus be related to the reflectivity/transmissivity (R_g/T_g) of the glass-air interface and to the single-pass transmission of the glass substrate (X_g) using the following equations

$$R_0 = R_g + \frac{R_g X_g^2 T_g^2}{1 - R_g^2 X_g^2} \quad (1)$$

$$T_0 = \frac{X_g T_g^2}{1 - R_g^2 X_g^2} \quad (2)$$

$$1 = R_g + T_g \quad (3)$$

These equations can be solved for R_g , T_g , and X_g . Since a thin film on a glass substrate is a multilayer system, additional assumptions are needed to process the film/glass spectra analytically. In this work, the refractive indices of the film and substrate were both expected to be ~ 1.5 , and thus, the reflection at the film-glass interface could be ignored without much distortion of the result. This simplification allowed for the raw reflection (R_1) and transmission (T_1) of the film/substrate to be incorporated into a similar set of equations as above while introducing only three new parameters

$$R_1 = R_f + \frac{R_g X_g^2 X_f^2 T_f^2}{1 - R_g R_f X_g^2 X_f^2} \quad (4)$$

$$T_1 = \frac{X_g X_f T_g T_f}{1 - R_g R_f X_g^2 X_f^2} \quad (5)$$

$$1 = R_f + T_f \quad (6)$$

In this second set of equations, R_f and T_f are the reflectivity and transmissivity of the film-air interface, respectively, and X_f is the single-pass transmission of the thin film. Solving these equations for X_f gives the corrected transmission of the thin film. The corresponding absorption of the film is

$$A_{\text{film}} = -\log(X_f) \quad (7)$$

This quantity can be calculated at each measured wavelength/energy to give the corrected absorption spectrum of the film at each of the seven measured positions.

Autonomous workflow step 6: Four-point probe conductance instrumentation and characterization

Four-point probe conductivity measurements were performed with a Keithley Series K2636B System SourceMeter instrument with a Signatone four-point probe head (part number SP4-40045TBN; 0.040-inch tip spacing, 45-g pressure, and tungsten carbide tips with 0.010-inch radii) connected through a Signatone triax to BNC feedthrough panel (part number TXBA-M160-M).

The current on the outer probes was stepped from 0 to 4 nA in 0.8-nA steps. The system was stabilized at each step for 0.5 s, and the potential across the inner probes was integrated for 25 power line cycles (at 60 Hz). The slope of the potential as a function of the current sourced afforded the resistance. No correction factors were applied to the resistance measurement, as the size of the slide is much larger than the spacing between the probes. The conductance of each film was measured at seven positions spaced ~ 1 mm apart near the

center of the substrate. These positions matched those used in spectroscopy measurements.

Autonomous workflow step 7: Pseudomobility calculation

Conventional theory describes the conductivity (σ) of p-type semiconductors as the product of the elementary charge (e), the density of positive charge carriers (ρ_h), and the mobility of these same charge carriers (μ). In numerous examples, ρ_h is treated as an independent variable programmed by doping fraction, while μ is an intrinsic material property found to vary with temperature, applied voltage, disorder, and doping fraction (22, 23). μ thus encompasses most of the complexity of σ and is often maximized to optimize the performance of electronic materials. In the specific case of an HTM, the doping fraction must be managed carefully given that underdoping reduces hole conductivity while overdoping risks depletion of valence electrons at the HTM/absorber interface that can lead to inefficient hole injection.

In this work, the value of μ for each HTM film was extracted from sheet resistance four-point probe and UV-vis measurements using the following methodology. The hole mobility of the HTM is expressed as

$$\mu_h = \frac{\sigma}{\rho_h e} \quad (8)$$

where the hole conductivity of the HTM is assumed to approximate the total conductivity due to the heavy p-doping of most measured conditions and the high intrinsic mobility of holes relative to that of electrons known to exist in spiro-OMeTAD. σ is defined as

$$\sigma = \frac{1}{R_s t} = \frac{\ln(2)}{R_s t} \frac{dV}{dI} \frac{1}{C \pi t} \quad (9)$$

where R_s is the sheet resistance, t is the film thickness, dV/dI is the linear change in voltage (V) with respect to current (I) at low V and I extracted from the four-point probe measurement, and C is a geometric correction factor tied to the ratio between the probe tip distances and the rectangular dimensions of the film. The redefinition of R_s here is valid for any four-point probe measurement in which t is much less than the distance between adjacent probe tips. ρ_h is defined as

$$\rho_h = \rho_{\text{HTM}} \frac{[\text{HTM}^+]}{[\text{HTM}]} \quad (10)$$

where ρ_{HTM} is the total density of redox active HTM sites in the film and $[\text{HTM}^+]/[\text{HTM}]$ is the fraction of active sites carrying a positive charge at any given time. This fraction is not necessarily equal to the ratio of dopant to HTM in the film since not all dopants oxidize HTM material quantitatively. ρ_{HTM} can be converted to a molar concentration by

$$\rho_{\text{HTM}} = 1000 N_A [\text{HTM}] \quad (11)$$

where N_A is the Avogadro constant and $1000 N_A$ is the unit of conversion between m^{-3} and M. The ratio of $[\text{HTM}^+]$ to $[\text{HTM}]$ is the same as the ratio of ρ_h to ρ_{HTM} . This yields

$$\rho_h = 1000 N_A [\text{HTM}^+] \quad (12)$$

which can be used in conjunction with Beer's law to incorporate data from the UV-vis spectrum of the film in question. The resulting equation

$$\rho_h = 1000 N_A \frac{A_{\text{HTM}^+}}{\epsilon t} = 1000 N_A \frac{A_{\text{film}}}{\epsilon t} \quad (13)$$

includes the molar extinction coefficient of the film (ϵ), the film thickness (t), and the reflection- and substrate-corrected absorbance (A_{HTM^+}) of the film in the wavelength range of 500 ± 5 nm, where all absorption can be attributed to HTM^+ . This final expression for ρ_h is only valid when the programmed dopant:HTM ratio is at or below 1:1 so that minimal HTM^{2+} exists in the film. Last, μ_h can be defined in terms of both experimental results

$$\mu_h = \frac{\sigma}{\rho_h e} = \left(\frac{\ln(2) \epsilon}{1000 \pi e C N_A} \right) \left(\frac{dI}{dV} \right) (A_{\text{HTM}^+})^{-1} \quad (14)$$

This expression is crucially independent of film thickness, allowing for accurate optimization over the full compositional and processing variable space used in this work. Dividing out the constants in the final equation above yields a parameter termed pseudomobility

$$\text{pseudomobility} = \left(\frac{dI}{dV} \right) (A_{\text{HTM}^+})^{-1} \quad (15)$$

Pseudomobility is equivalent to the quotient of film conductivity and p-type carrier density and provides a useful measure of relative mobility that can be used in optimization experiments. The pseudomobility of each thin film was calculated independently at each of the seven characterized positions. The pseudomobility value passed to the optimization algorithm was the mean value of the seven positional pseudomobilities.

Autonomous workflow step 8: Determining the next experiment with Bayesian optimization

After each thin film experiment, the realized experimental parameters and resulting pseudomobility value were sent to an instance of ChemOS (14) running on a remote server via a file transfer interface (Dropbox). ChemOS then provided the experimental data to the Phoenix (15) global Bayesian optimization algorithm, initiating an update of the algorithm's surrogate model of the experimental response surface. To minimize the robot's downtime between the completion of one experiment and the initiation of the next experiment, ChemOS immediately provides parameters for the next experiment, which have been precomputed by Phoenix. In this way, the moderately computationally intensive updating of Phoenix's surrogate model can occur in parallel with the robotic execution of the next experiment, shortening the execution of a campaign with 30 experiments by about 30 min. Phoenix suggests new experiments by using an adjustable sampling parameter to explicitly bias experimental design toward exploration or exploitation in an alternating fashion and thus enables global optimization over the response surfaces explored by the robotic platform. The initial sample is chosen at random, as no model of the response surface is initially available. The exchange of information between ChemOS and the robotic platform is managed by Python software written in-house.

SUPPLEMENTARY MATERIALS

Supplementary material for this article is available at <http://advances.sciencemag.org/cgi/content/full/6/20/eaaz8867/DC1>

REFERENCES AND NOTES

1. A. Aspuru-Guzik, K. Persson, A. Alexander-Katz, C. Amador, D. Solis-Ibarra, M. Antes, A. Mosby, M. Aykol, E. Chan, S. Dwaraknath, J. Montoya, E. Rotenberg, J. Gregoire, J. Hatrick-Simpers, D. M. Huang, J. Hein, G. Hutchison, O. Isayev, Y. Jung, J. Kiviahio, C. Kreisbeck, L. Roch, S. Saikin, D. Tabor, J. Lambert, S. Odom, J. Pijpers, M. Ross, J. Schrier, R. Segal, M. Sfeir, H. Tribukait, T. Vegge, *Materials Acceleration Platform: Accelerating Advanced Energy Materials Discovery by Integrating High-Throughput Methods and Artificial Intelligence* (Mission Innovation Clean Energy Materials Innovation Challenge, 2018); <http://nrs.harvard.edu/urn-3:HUL.InstRepos:35164974>.
2. J.-P. Correa-Baena, K. Hippalgaonkar, J. van Duren, S. Jaffer, V. R. Chandrasekhar, V. Stevanovic, C. Wadia, S. Guha, T. Buonassisi, Accelerating materials development via automation, machine learning, and high-performance computing. *Joule* **2**, 1410–1420 (2018).
3. B. Cao, L. A. Adutwum, A. O. Olynyk, E. J. Luber, B. C. Olsen, A. Mar, J. M. Buriak, How to optimize materials and devices via design of experiments and machine learning: Demonstration using organic photovoltaics. *ACS Nano* **12**, 7434–7444 (2018).
4. X. D. Xiang, X. Sun, G. Briceño, Y. Lou, K. A. Wang, H. Chang, W. G. Wallace-Freedman, S. W. Chen, P. G. Schultz, A combinatorial approach to materials discovery. *Science* **268**, 1738–1740 (1995).
5. H. S. Stein, D. Guevarra, P. F. Newhouse, E. Soedarmadji, J. M. Gregoire, Machine learning of optical properties of materials - predicting spectra from images and images from spectra. *Chem. Sci.* **10**, 47–55 (2019).
6. F. Häse, L. M. Roch, A. Aspuru-Guzik, Next-generation experimentation with self-driving laboratories. *Trends in Chemistry* **1**, 282–291 (2019).
7. J. Li, Y. Lu, Y. Xu, C. Liu, Y. Tu, S. Ye, H. Liu, Y. Xie, H. Qian, X. Zhu, AIR-Chem: Authentic intelligent robotics for chemistry. *J. Phys. Chem. A* **122**, 9142–9148 (2018).
8. Y. Bai, L. Wilbraham, B. J. Slater, M. A. Zwijsburg, R. S. Sprick, A. I. Cooper, Accelerated discovery of organic polymer photocatalysts for hydrogen evolution from water through the integration of experiment and theory. *J. Am. Chem. Soc.* **141**, 9063–9071 (2019).
9. V. Gopalaswamy, R. Betti, J. P. Knauer, N. Luciani, D. Patel, K. M. Woo, A. Bose, I. V. Igumenshchev, E. M. Campbell, K. S. Anderson, K. A. Bauer, M. J. Bonino, D. Cao, A. R. Christopherson, G. W. Collins, T. J. B. Collins, J. R. Davies, J. A. Delettretz, D. H. Edgell, R. Epstein, C. J. Forrest, D. H. Froula, V. Y. Glebov, V. N. Goncharov, D. R. Harding, S. X. Hu, D. W. Jacobs-Perkins, R. T. Janezic, J. H. Kelly, O. M. Mannion, A. Maximov, F. J. Marshall, D. T. Michel, S. Miller, S. F. B. Morse, J. Palastro, J. Peebles, P. B. Radha, S. P. Regan, S. Sampat, T. C. Sangster, A. B. Sefkow, W. Seka, R. C. Shah, W. T. Shmyada, A. Shvydky, C. Stoeckl, A. A. Solodov, W. Theobald, J. D. Zuegel, M. G. Johnson, R. D. Petrasso, C. K. Li, J. A. Freije, Tripled yield in direct-drive laser fusion through statistical modelling. *Nature* **565**, 581–586 (2019).
10. J. Granda, L. Donina, V. Dragone, D.-L. Long, L. Cronin, Controlling an organic synthesis robot with machine learning to search for new reactivity. *Nature* **559**, 377–381 (2018).
11. R. D. King, K. E. Whelan, F. M. Jones, P. G. K. Reiser, C. H. Bryant, S. H. Muggleton, D. B. Kell, S. G. Oliver, Functional genomic hypothesis generation and experimentation by a robot scientist. *Nature* **427**, 247–252 (2004).
12. P. Nikolaev, D. Hooper, N. Perea-López, M. Terrones, B. Maruyama, Discovery of wall-selective carbon nanotube growth conditions via automated experimentation. *ACS Nano* **8**, 10214–10222 (2014).
13. F. Ren, L. Ward, T. Williams, K. J. Laws, C. Wolverton, J. Hatrick-Simpers, A. Mehta, Accelerated discovery of metallic glasses through iteration of machine learning and high-throughput experiments. *Sci. Adv.* **4**, eaq1566 (2018).
14. L. Meng, Y. Zhang, X. Wan, C. Li, X. Zhang, Y. Wang, X. Ke, Z. Xiao, L. Ding, R. Xia, H.-L. Yip, Y. Cao, Y. Chen, Organic and solution-processed tandem solar cells with 17.3% efficiency. *Science* **361**, 1094–1098 (2018).
15. A. S. D. Sandanayaka, T. Matsushima, F. Bencheikh, S. Terakawa, W. J. Potscavage Jr., C. Qin, T. Fujihara, K. Goushi, J.-C. Ribierre, C. Adachi, Indication of current-injection lasing from an organic semiconductor. *Appl. Phys. Express* **12**, 061010 (2019).
16. S. Jhulki, J. N. Moorthy, Small molecular hole-transporting materials (HTMs) in organic light-emitting diodes (OLEDs): Structural diversity and classification. *J. Mater. Chem. C* **6**, 8280–8325 (2018).
17. X. Yang, H. Wang, B. Cai, Z. Yu, L. Sun, Progress in hole-transporting materials for perovskite solar cells. *J. Energy Chem.* **27**, 650–672 (2018).
18. J. Burschka, F. Kessler, M. K. Nazeeruddin, M. Grätzel, Co(III) complexes as p-dopants in solid-state dye-sensitized solar cells. *Chem. Mater.* **25**, 2986–2990 (2013).
19. S. Wang, M. Sina, P. Parikh, T. Uekert, B. Shahbazian, A. Devaraj, Y. S. Meng, Role of 4-tert-butylpyridine as a hole transport layer morphological controller in perovskite solar cells. *Nano Lett.* **16**, 5594–5600 (2016).
20. T. Bu, L. Wu, X. Liu, X. Yang, P. Zhou, X. Yu, T. Qin, J. Shi, S. Wang, S. Li, Z. Ku, Y. Peng, F. Huang, Q. Meng, Y.-B. Cheng, J. Zhong, Synergic interface optimization with green solvent engineering in mixed perovskite solar cells. *Adv. Energy Mater.* **7**, 1700576 (2017).
21. Y. Fang, X. Wang, Q. Wang, J. Huang, T. Wu, Impact of annealing on spiro-OMeTAD and corresponding solid-state dye sensitized solar cells. *Phys. Status Solidi* **211**, 2809–2816 (2014).

22. C. Liu, K. Huang, W.-T. Park, M. Li, T. Yang, X. Liu, L. Liang, T. Minari, Y.-Y. Noh, A unified understanding of charge transport in organic semiconductors: The importance of attenuated delocalization for the carriers. *Mater. Horiz.* **4**, 608–618 (2017).
23. Y. Shen, K. Diest, M. H. Wong, B. R. Hsieh, D. H. Dunlap, G. G. Malliaras, Charge transport in doped organic semiconductors. *Phys. Rev. B* **68**, 081204 (2003).
24. Z. H. Bakr, Q. Wali, A. Fakharuddin, L. Schmidt-Mende, T. M. Brown, R. Jose, Advances in hole transport materials engineering for stable and efficient perovskite solar cells. *Nano Energy* **34**, 271–305 (2017).
25. P. Friederich, V. Meded, A. Poschlad, T. Neumann, V. Rodin, V. Stehr, F. Symalla, D. Danilov, G. Lüdemann, R. F. Fink, I. Kondov, F. von Wrochem, W. Wenzel, Molecular origin of the charge carrier mobility in small molecule organic semiconductors. *Adv. Funct. Mater.* **26**, 5757–5763 (2016).
26. L. M. Roch, F. Häse, C. Kreisbeck, T. Tamayo-Mendoza, L. P. E. Yunker, J. E. Hein, A. Aspuru-Guzik, ChemOS: Orchestrating autonomous experimentation. *Sci. Robot.* **3**, eaat5559 (2018).
27. F. Häse, L. M. Roch, C. Kreisbeck, A. Aspuru-Guzik, Phoenix: A Bayesian optimizer for chemistry. *ACS Cent. Sci.* **4**, 1134–1145 (2018).
28. F. Häse, L. M. Roch, A. Aspuru-Guzik, Chimera: Enabling hierarchy based multi-objective optimization for self-driving laboratories. *Chem. Sci.* **9**, 7642–7655 (2018).
29. J. C. Blakesley, F. A. Castro, W. Kylberg, G. F. A. Dibb, C. Arantes, R. Valaski, M. Cremona, J. S. Kim, J.-S. Kim, Towards reliable charge-mobility benchmark measurements for organic semiconductors. *Org. Electron.* **15**, 1263–1272 (2014).
30. B. Xu, H. Tian, L. Lin, D. Qian, H. Chen, J. Zhang, N. Vlachopoulos, G. Boschloo, Y. Luo, F. Zhang, A. Hagfeldt, L. Sun, Integrated design of organic hole transport materials for efficient solid-state dye-sensitized solar cells. *Adv. Energy Mater.* **5**, 1401185 (2015).
31. R. E. Brandt, R. C. Kurchin, V. Steinmann, D. Kitchaev, C. Roat, S. Levenco, G. Ceder, T. Unold, T. Buonassisi, Rapid photovoltaic device characterization through bayesian parameter estimation. *Joule* **1**, 843–856 (2017).
32. T. H. Schloemer, J. A. Christians, J. M. Luther, A. Sellinger, Doping strategies for small molecule organic hole-transport materials: Impacts on perovskite solar cell performance and stability. *Chem. Sci.* **10**, 1904–1935 (2019).
33. T. Malinauskas, D. Tomkute-Luksiene, R. Sens, M. Daskeviciene, R. Send, H. Wonneberger, V. Jankauskas, I. Bruder, V. Getautis, Enhancing thermal stability and lifetime of solid-state dye-sensitized solar cells via molecular engineering of the hole-transporting material spiro-OMeTAD. *ACS Appl. Mater. Interfaces* **7**, 11107–11116 (2015).
34. J.-Y. Seo, H.-S. Kim, S. Akin, M. Stojanovic, E. Simon, M. Fleischer, A. Hagfeldt, S. M. Zakeeruddin, M. Grätzel, Novel p-dopant toward highly efficient and stable perovskite solar cells. *Energ. Environ. Sci.* **11**, 2985–2992 (2018).
35. Q. Wang, Influence of a cobalt additive in spiro-OMeTAD on charge recombination and carrier density in perovskite solar cells investigated using impedance spectroscopy. *Phys. Chem. Chem. Phys.* **20**, 10114–10120 (2018).
36. A.-C. Bédard, A. Adamo, K. C. Aroh, M. G. Russell, A. A. Bedermann, J. Torosian, B. Yue, K. F. Jensen, T. F. Jamison, Reconfigurable system for automated optimization of diverse chemical reactions. *Science* **361**, 1220–1225 (2018).
37. P. J. Kitson, G. Marie, J.-P. Francoia, S. S. Zalesskiy, R. C. Sigerson, J. S. Mathieson, L. Cronin, Digitization of multistep organic synthesis in reactionware for on-demand pharmaceuticals. *Science* **359**, 314–319 (2018).

Acknowledgment: We would like to acknowledge M. Eghtesad for contributions to the project hardware and experimentation and T. Zepel for contributions in literature research. We thank the UBC Chemistry machine shop for assistance with instrument fabrication. We would like to acknowledge CMC Microsystems for the provision of products and services that facilitated this research, including SolidWorks 2018 SP5.0. For robot control and data processing, we would like to acknowledge the contributors to the Python programming language (Python Software Foundation; <https://python.org>). **Funding:** The authors thank Natural Resources Canada (EIP2-MAT-001) for financial support. C.P.B. is grateful to the Natural Sciences and Engineering Research Council of Canada (NSERC; RGPIN 337345-13), the Canadian Foundation for Innovation (229288), the Canadian Institute for Advanced Research (BSE-BERL-162173), and the Canada Research Chairs Program for financial support. B.P.M., F.G.L.P., T.D.M., and C.P.B. acknowledge support from the SBQMI's Quantum Electronic Science and Technology Initiative, the Canada First Research Excellence Fund, and the Quantum Materials and Future Technologies Program. J.E.H. is supported by the NSERC (RGPIN 2016-04613) and Canada Foundation for Innovation (35833). V.L. and H.S. were supported by an NSERC Strategic Partnership Grant (STPGP 493833-16). F.H. acknowledges support from the Herchel Smith Graduate Fellowship and the Jacques-Emile Dubois Student Dissertation Fellowship. L.M.R. and A.A.-G. were supported by the Tata Sons Limited Alliance Agreement (A32391) and the Office of Naval Research (N00014-19-1-2134) and would also like to thank A. Frøseth for support. **Author contributions:** A.A.-G., J.E.H., and C.P.B. conceived and supervised the project. B.P.M., M.B.R., H.S., G.J.N., R.H.Z., and F.G.L.P. developed the robotic hardware. F.G.L.P., T.D.M., J.R.D., T.H.H., and B.P.M. developed the data analysis software. L.P.E.Y., B.P.M., F.G.L.P., G.J.N., R.H.Z., V.L., M.S.E., K.E.D., and H.S. developed the robotic control software. F.H., L.M.R., and A.A.-G. developed the optimization algorithm and interfaced the algorithm with the robot. F.G.L.P., T.D.M., B.P.M., K.E.D., F.H., and L.M.R. designed and performed the robotic optimization experiments. T.D.M., M.S.E., and D.J.D. performed additional experiments. All authors participated in the writing of the manuscript. **Competing interests:** The authors declare that they have no competing interests. **Data and material availability:** All data needed to evaluate the conclusions in the paper are present in the paper and/or the Supplementary Materials. The raw data recorded by the robotic platform during the two optimization runs are available at <https://github.com/berlinguette/ada>. Additional data related to this paper may be requested from the authors.

Submitted 16 October 2019

Accepted 28 February 2020

Published 13 May 2020

10.1126/sciadv.aaz8867

Citation: B. P. MacLeod, F. G. L. Parlane, T. D. Morrissey, F. Häse, L. M. Roch, K. E. Dettelbach, R. Moreira, L. P. E. Yunker, M. B. Rooney, J. R. Deeth, V. Lai, G. J. Ng, H. Situ, R. H. Zhang, M. S. Elliott, T. H. Haley, D. J. Dvorak, A. Aspuru-Guzik, J. E. Hein, C. P. Berlinguette, Self-driving laboratory for accelerated discovery of thin-film materials. *Sci. Adv.* **6**, eaaz8867 (2020).

Self-driving laboratory for accelerated discovery of thin-film materials

B. P. MacLeod, F. G. L. Parlane, T. D. Morrissey, F. Häse, L. M. Roch, K. E. Dettelbach, R. Moreira, L. P. E. Yunker, M. B. Rooney, J. R. Deeth, V. Lai, G. J. Ng, H. Situ, R. H. Zhang, M. S. Elliott, T. H. Haley, D. J. Dvorak, A. Aspuru-Guzik, J. E. Hein and C. P. Berlinguette

Sci Adv **6** (20), eaaz8867.
DOI: 10.1126/sciadv.aaz8867

ARTICLE TOOLS

<http://advances.sciencemag.org/content/6/20/eaaz8867>

SUPPLEMENTARY MATERIALS

<http://advances.sciencemag.org/content/suppl/2020/05/11/6.20.eaaz8867.DC1>

REFERENCES

This article cites 36 articles, 5 of which you can access for free
<http://advances.sciencemag.org/content/6/20/eaaz8867#BIBL>

PERMISSIONS

<http://www.sciencemag.org/help/reprints-and-permissions>

Use of this article is subject to the [Terms of Service](#)

Science Advances (ISSN 2375-2548) is published by the American Association for the Advancement of Science, 1200 New York Avenue NW, Washington, DC 20005. The title *Science Advances* is a registered trademark of AAAS.

Copyright © 2020 The Authors, some rights reserved; exclusive licensee American Association for the Advancement of Science. No claim to original U.S. Government Works. Distributed under a Creative Commons Attribution NonCommercial License 4.0 (CC BY-NC).